the dynamic process of dissociative adsorption of an H_2 molecule above graphene surface.

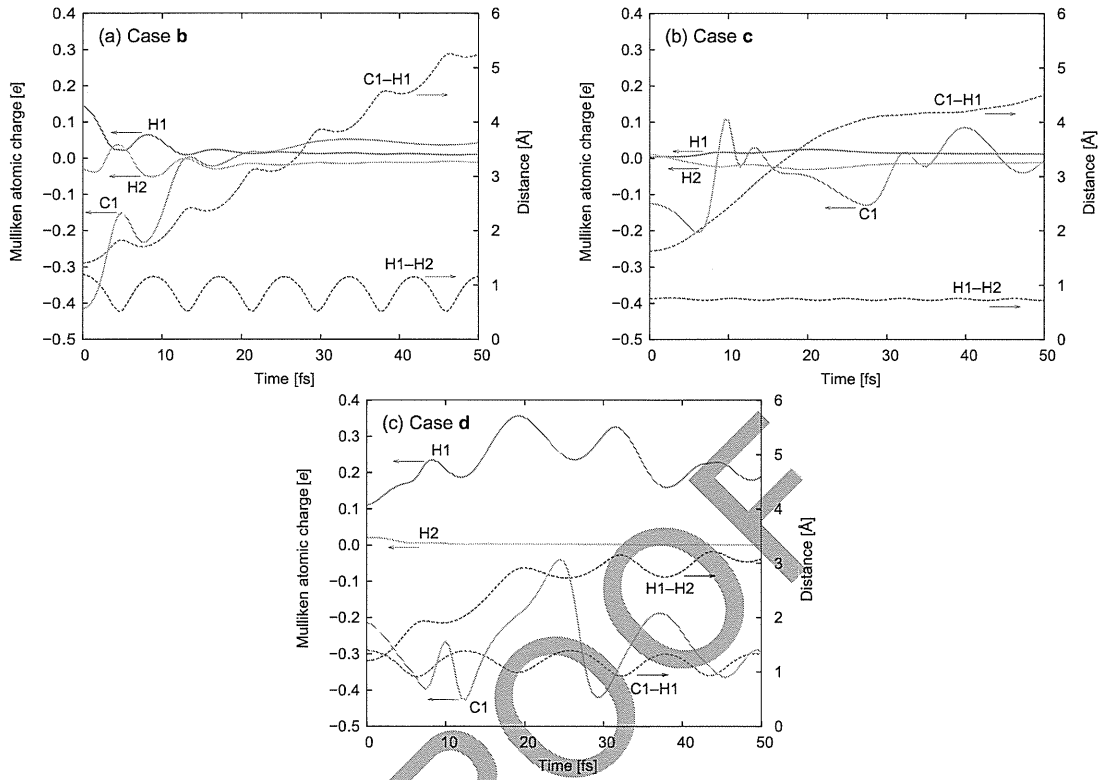

Figure 7: Transitions of Mulliken atomic charge of C1, H1, and H2 (solid lines) and of C1–H1 and H1–H2 lengths (dashed lines) for initial conditions of (a) **b**, (b) **c**, and (c) **d**.

Figures 7 and 8 describe the dynamic process of dissociative adsorption of an H_2 molecule as follows. First, electrons on the H_2 molecule move toward the graphene surface, inducing polarization between the H_2 molecule and the graphene. Second, repulsive interactions are enhanced between the H1 and H2 atoms, which have weakly positive charges (see Fig. 7(c)). On the other hand, the C1 atom which accepts electrons from the H_2 molecule, attracts one of the H atoms and forms a chemical bond with H1. Third, the electrons on C1 move back to H1 after the C1–H1 bond shrinks (see Figs. 7(c) and 8). Finally, the H2 atom located furthest side from the graphene surface leaves in an electrically neutral condition. In this period, the positively charged H2 seems to recieve electrons from the negatively charged C1. The periodic vibration between the adsorbed H1 and C1 atoms is conserved due to the periodic charge transfer between them.

In the present study, the existence of a critical pathway in the dissociative adsorp-

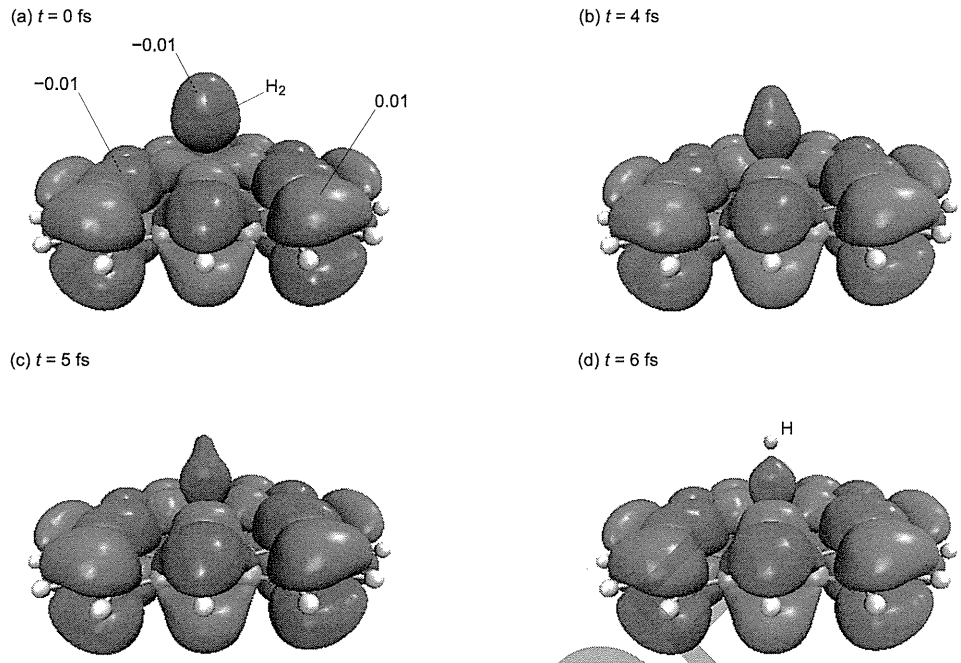

Figure 8: Snapshots of a molecular orbital which focuses on H_2 during *ab initio* MD simulation with HF/3-21G(d,p) level at (a) 0 s, (b) 4.0 fs, (c) 5.0 fs, and (d) 6.0 fs; isosurfaces of the molecular orbital correspond to the values of 0.01 and -0.01.

tion of an H_2 molecule on a graphene layer was suggested as a result of many trials. In a precise sense, all possible trajectories which depend on the initial conditions, temperature, and pressure should be investigated. However, there are many difficulties to satisfy the actual experimental conditions. The present study has found out one of important results in all possiblities. The knowledges obtained from the simulations are very meaningful and motivate more detailed investigations, even though they are resulted from the excessively excited conditions. In the next section, the potential energy surface (PES) analysis is performed to clarify a whole reaction pathway which was partly found out by *ab initio* MD simulations.

3.3 Potential energy analysis on the reaction pathway

In this section, the validity of the *ab initio* MD results for condition **d** is discussed and critical reaction pathways will be elucidated according to the manner of quantum chemistry. A purpose of this section is to explain the nature of dissociative adsorption of H_2 on grapene surfaces. The PESs for the static system between $C_{37}H_{15}$+H_2 and $C_{37}H_{16}$+H were investigated. In this analysis, the 6-31G(d,p) basis set was adopted instead of the 3-21G(d,p) basis set which was used for the *ab*

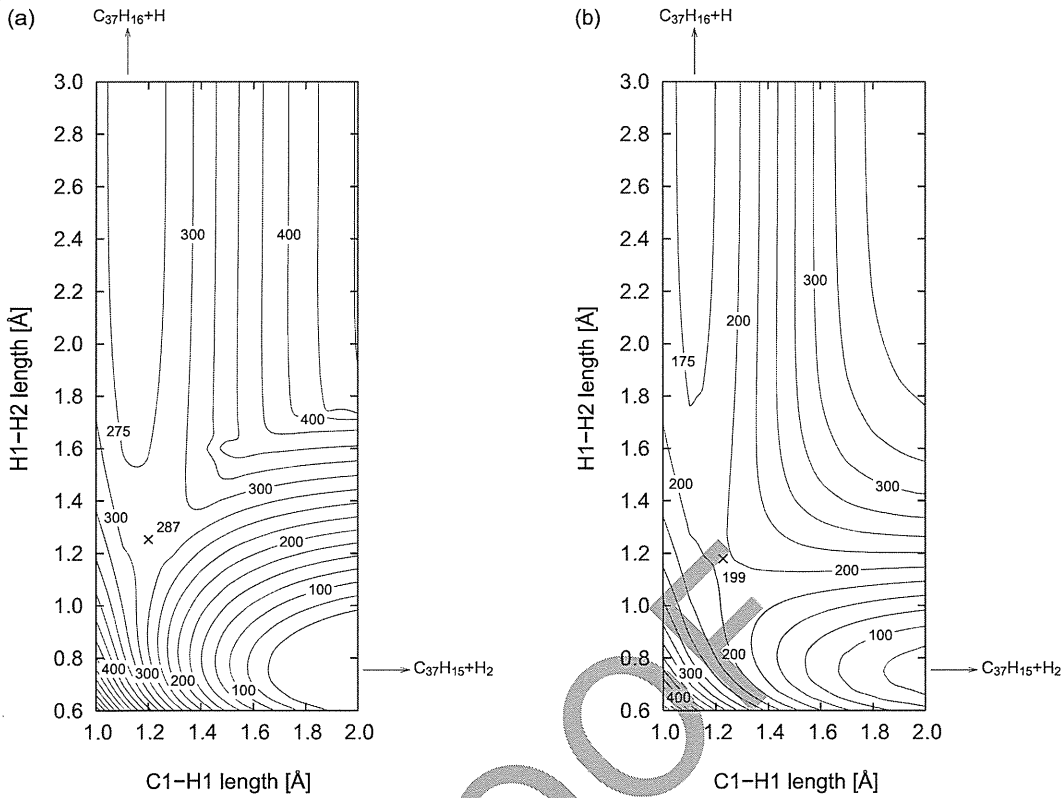

Figure 9: Potential energy surface of H_2 molecule above (a) planar graphene ($h = 0.0$ Å) and (b) steric site on graphene ($h = 0.25$ Å), in which the saddle points are indicated by $\times$ at the location of (a) $(x,y) = (1.20, 1.25)$ and (b) $(x,y) = (1.23, 1.18)$; x and y axes represent C1–H1 length and H1–H2 length, respectively. Values written in the unit of kJ/mol are measured from the reference state of $C_{37}H_{15}$+H_2.

initio MD computations. It is for the higher accuracy and for the quantitative comparison with the previous works [Elias, Nair, Mohiuddin, Morozov, Blake, Halsall, Ferrari, Boukhvalov, Katsnelson, Geim, and Novoselov (2009); Sha and Jackson (2001)]. The difference of basis sets was confirmed to be less effective for the H_2 dissociation process. However, the dissociative adsorption process of an H_2 molecule was limited near a graphene surface where electron transfers between the two molecules induced the reaction, because the dissociation limit on a continuous PES should not be discussed by the HF approximation. Figure 9 shows the contour maps of the relative potential energy with respect to interactions between an H_2 molecule and a graphene surface as a function of C1–H1 and H1–H2 lengths. The relative energies were measured from the isolated condition of an H_2 molecule and a graphene: $C_{37}H_{15}$+H_2. The C1 atom located at the center of graphene was

elevated from the planar surface by $h = 0.25$ Å as well as the case of $h = 0$ Å. Although this height is lower than that of condition **d**, it seems to be more realistic [Elias, Nair, Mohiuddin, Morozov, Blake, Halsall, Ferrari, Boukhvalov, Katsnelson, Geim, and Novoselov (2009); Sha and Jackson (2001)] from the viewpoint of stability. Figure 9(a) shows the contour map of the case of $h = 0$ Å. It is found that there are steeps along the directions to shorten the C1–H1 length and to stretch the H1–H2 length and that an H_2 molecule located far from the graphene surface is stable. A cross mark in the map is considered to be a saddle point in the reaction pathway between $C_{37}H_{15}$+H_2 and $C_{37}H_{16}$+H. The energy difference between the dissociation limit of $C_{37}H_{15}$+H_2 and the saddle point shows that an activation energy of 287 kJ/mol (2.98 eV) is required to cleave an H_2 molecule. On the other hand, the other local minimum of $C_{37}H_{16}$+H is very shallow and gradients around it are moderate. This result means that quite-high energy should be provided to cleave the H1–H2 bond and that the excessively high energy will negatively contribute to the repulsion between the H atoms and the graphene. Therefore, it will be difficult to realize the dissociative adsorption of H_2 molecules on planar graphene surfaces. Figure 9(b) shows the result about the case of $h = 0.25$ Å, that is, the case of steric graphene surface. It is found that gradients around the stable state of $C_{37}H_{15}$+H_2 appear to be more moderate than those in Fig. 9(a). The energy required to cleave the H1–H2 bond evaluated as 199 kJ/mol (2.06 eV). This value is 88 kJ/mol (0.92 eV) lower than the activation energy evaluated on the planar graphene surface. These moderate gradients enable the successive dissociation and adsorption of H_2. Additionally, the saddle points in the other cases of $h = 0.50$, 0.75, and 1.00 Å were evaluated as 252 kJ/mol (2.61 eV), 450 kJ/mol (4.66 eV), and 760 kJ/mol (7.88 eV), respectively, although their PESs are omitted here. It is predicted that the activation energy increases as h increases and that infinitesimal distortions of graphene surfaces are effective to decrease the activation energy of H_2 dissociation. In comparison with the present result, the dissociation energy of an H_2 molecule in vacuum without graphene was estimated here to be 354 kJ/mol (3.67 eV), which was in reasonable agreement with the experimental value of 432 kJ/mol (4.48 eV) [Herzberg (1969)]. That is, in the case of $h = 0.25$ Å, the dissociation energy of H_2 above graphene is estimated as 155 kJ/mol (1.61 eV) lower than that without graphene. Consequently, steric C sites on the graphene surface are expected to act as a catalytic agent. Both previous results for an H atom near a carbon surface [Jeloacia and Sidis (1999)] and the present results for an H_2 molecule strongly indicate the feasibility of using a distorted carbon material for hydrogen storage materials.

In practical applications, external energy estimations are required to form steric sites which distort the planar graphene surface and to move the H_2 molecule toward

the surface. More accurate energy estimations will be possible using the density functional theory, the multi-configurational self-consistent field, or the configuration interactions [Szabo and Ostlund (1982)]. However, as a first step, we carried out the present *ab initio* MD analysis to investigate the dissociative adsorption process of H_2 molecules, focusing on the molecular dynamics, the Mulliken atomic charges, and molecular orbitals.

4 Conclusion

In the present study, an *ab initio* MD method with wave function convergences was developed and used to investigate the time-dependent behavior of an H_2 molecule above a graphene surface. The simulations could quantitatively evaluate a scenario in which distorted graphene surfaces enhanced H_2 dissociation and an H atom adsorption at the steric sites. In conjunction with this *ab initio* MD simulations, the potential energy surface analysis was also applied to clarify the detailed dissociative adsorption process of an H_2 molecule. Important conclusions obtained from this study are summarized below.

1. Focusing on dissociative adsorption of H_2 on a graphene surface, the time-dependent phenomena were clarified by the present procedure. In particular, sequential electron transfers from H_2 to C and from C to 2H were indicated. The former process dominated H_2 dissociation and the latter one dominated the subsequent C–H adsorption with the dissociation of a neutral H atom. Furthermore, the periodic electron transfer which was synchronized with the C–H vibration was predicted.

2. Based on the *ab initio* MD results, a critical reaction pathway for the dissociative adsorption was determined. The calculations in the present study suggest that H_2 dissociation can be realized above the distorted graphene surface with an activation energy of 199 kJ/mol (2.06 eV), which is lower than that in vacuum without graphene. However, the same process is not expected to occur on a planar surface because the dissociation limit of $C_{37}H_{15}$+H_2 is so stable that quite-high energies to induce the dissociative adsorption negatively cause repulsions between H atoms and a graphene surface.

3. The dissociation energy of an H–H bond near the steric configuration of C atoms was expected to be reduced to 56.2 % of that without graphene. This result highlights the capacity of distorted graphene to be avaliable as a catalytic agent which does not require expensive materials such as Pt. Furthermore, by exploiting the subsequent C–H adsorption, steric graphene surfaces are promising candidates for hydrogen storages.

References

Allen, M. P.; Tildesley, D. J. (1989): *Computer Simulation of Liquids*. Oxford University Press, Clarendon, Oxford.

Arellano, J. S.; Molina, L. M.; Rubio, A.; Alonso, J. A. (2000): Density functional study of adsorption of molecular hydrogen on graphene layers. *J. Chem. Phys.*, vol. 112, pp. 8114–8119.

Berseth, P. A.; Harter, A. G.; Zidan, R.; Blomqvist, A.; Araújo, C. M.; Scheicher, R. H.; Ahuja, R.; Jena, P. (2009): Carbon nanomaterials as catalysts for hydrogen uptake and release in $NaAlH_4$. *Nano Lett.*, vol. 9, pp. 1501–1505.

Chan, S.-P.; Chen, G.; Gong, X. G.; Liu, Z.-F. (2001): Chemisorption of hydrogen molecules on carbon nanotubes under high pressure. *Phys. Rev. Lett.*, vol. 87, pp. 205502–1–205502–4.

Chen, P.; Wu, X.; Lin, J.; Tan, K. L. (1999): High H_2 uptake by alkali-doped carbon nanotubes under ambient pressure and moderate temperatures. *Science*, vol. 285, pp. 91–93.

Chen, Y.; Shaw, D. T.; Bai, X. D.; Wang, E. G.; Lund, C.; Lu, W. M.; Chung, D. D. L. (2001): Hydrogen storage in aligned carbon nanotubes. *Appl. Phys. Lett.*, vol. 78, pp. 2128–2130.

Cheng, H.; Pez, G.; Kern, G.; Kresse, G.; Hafner, J. (2001): Hydrogen adsorption in potassium-intercalated graphite of second stage: an *ab initio* molecular dynamics study. *J. Phys. Chem. B*, vol. 105, pp. 736–742.

Cheng, H.; Pez, G. P.; Cooper, A. C. (2003): Spontaneous cross linking of small-diameter single-walled carbon nanotubes. *Nano Lett.*, vol. 3, pp. 585–587.

Deumens, E.; Diz, A.; Longo, R.; Öhrn, Y. (1994): Time-dependent theoretical treatments of the dynamics of electrons and nuclei in molecular systems. *Rev. Mod. Phys.*, vol. 66, pp. 917–983.

Dillon, A. C.; Jones, K. M.; Bekkedahl, T. A.; Kiang, C. H.; Bethune, D. S.; Heben, M. J. (1997): Storage of hydrogen in single-walled carbon nanotubes. *Nature*, vol. 386, pp. 377–379.

Doi, K.; Haga, T.; Shintaku, H.; Kawano, S. (2010): Development of coarse-graining DNA models for single-nucleotide resolution analysis. *Phil. Trans. R. Soc. A*, vol. 368, pp. 2615–2628.

Doi, K.; Nakano, H.; Ohta, H.; Tachibana, A. (2007): First-principle molecular-dynamics study of hydrogen and aluminum nanowires in carbon nanotubes. *Mater. Sci. Forum*, vol. 539–543, pp. 1409–1414.

Durgun, E.; Ciraci, S.; Yildirim, T. (2008): Functionalization of carbon-based nanostructures with light transition-metal atoms for hydrogen storage. *Phys. Rev. B*, vol. 77, pp. 085405–1–085405–9.

Elias, D. C.; Nair, R. R.; Mohiuddin, T. M. G.; Morozov, S. V.; Blake, P.; Halsall, M. P.; Ferrari, A. C.; Boukhvalov, D. W.; Katsnelson, M. I.; Geim, A. K.; Novoselov, K. S. (2009): Control of graphene's properties by reversible hydrogenation: evidence for graphane. *Science*, vol. 323, pp. 610–613.

Feynman, R. P. (1939): Forces in molecules. *Phys. Rev.*, vol. 56, pp. 340–343.

Frisch, M. J.; Trucks, G. W.; Schlegel, H. B.; Scuseria, G. E.; Robb, M. A.; Cheeseman, J. R.; Montgomery Jr, J. A.; Vreven, T.; Kudin, K. N.; Burant, J. C.; Millam, J. M.; Iyengar, S. S.; Tomasi, J.; Barone, V.; Mennucci, B.; Cossi, M.; Scalmani, G.; Rega, N.; Petersson, G. A.; Nakatsuji, H.; Hada, M.; Ehara, M.; Toyota, K.; Fukuda, R.; Hasegawa, J.; Ishida, M.; Nakajima, T.; Honda, Y.; Kitao, O.; Nakai, H.; Klene, M.; Li, X.; Knox, J. E.; Hratchian, H. P.; Cross, J. B.; Adamo, C.; Jaramillo, J.; Gomperts, R.; Stratmann, R. E.; Yazyev, O.; Austin, A. J.; Cammi, R.; Pomelli, C.; Ochterski, J. W.; Ayala, P. Y.; Morokuma, K.; Voth, G. A.; Salvador, P.; Dannenberg, J. J.; Zakrzewski, V. G.; Dapprich, S.; Daniels, A. D.; Strain, M. C.; Farkas, O.; Malick, D. K.; Rabuck, A. D.; Raghavachari, K.; Foresman, J. B.; Ortiz, J. V.; Cui, Q.; Baboul, A. G.; Clifford, S.; Cioslowski, J.; Stefanov, B. B.; Liu, G.; Liashenko, A.; Piskorz, P.; Komaromi, I.; Martin, R. L.; Fox, D. J.; Keith, T.; Al-Laham, M. A.; Peng, C. Y.; Nanayakkara, A.; Challacombe, M.; Gill, P. M. W.; Johnson, B.; Chen, W.; Wong, M. W.; Gonzalez, C.; Pople, J. A. (2004): computer code GAUSSIAN 03 Rev. D.01, 2004.

Guisineger, N. P.; Rutter, G. M.; Crain, J. N.; First, P. N.; Stroscio, J. A. (2009): Exposure of epitaxial graphene on SiC(0001) to atomic hydrogen. *Nano Lett.*, vol. 9, pp. 1462–1466.

Gupta, B. K.; Srivastava, O. N. (2000): Synthesis and hydrogenation behaviour of graphitic nanofibres. *Int. J. Hydrogen Energy*, vol. 25, pp. 825–830.

Gupta, B. K.; Srivastava, O. N. (2001): Further studies on microstructural characterization and hydrogenation behaviour of graphitic nanofibres. *Int. J. Hydrogen Energy*, vol. 26, pp. 857–862.

Hanasaki, I.; Nakamura, A.; Yonebayashi, T.; Kawano, S. (2008): Structure and stability of water chain in a carbon nanotube. *J. Phys. Condens. Matter.*, vol. 20, pp. 015213–1–015213–7.

Herzberg, G. (1969): Dissociation energy and ionization potential of molecular hydrogen. *Phys. Rev. Lett.*, vol. 23, pp. 1081–1083.

Hirscher, M.; Becher, M.; Haluska, M.; Dettlaff-Weglikowska, U.; Quintel, A.; Duesberg, G. S.; Choi, Y.-M.; Downes, P.; Hulman, M.; Roth, S.; Stepanek, I.; Bernier, P. (2001): Hydrogen storage in sonicated carbon materials. *Appl. Phys. A*, vol. 72, pp. 129–132.

Jeloacia, L.; Sidis, V. (1999): DFT investigation of the adsorption of atomic hydrogen on a cluster-model graphite surface. *Chem. Phys. Lett.*, vol. 300, pp. 157–162.

Kawano, S. (1998): Molecular dynamics of rupture phenomena in a liquid thread. *Phys. Rev. E*, vol. 58, pp. 4468–4472.

Leforestier, C. (1978): Classical trajectories using the full *ab initio* potential energy surface $H^-+CH_4 \rightarrow CH_4+H^-$. *J. Chem. Phys.*, vol. 68, pp. 4406–4410.

Li, J.; Furuta, T.; Goto, H.; Ohashi, T.; Fujiwara, Y.; Yip, S. (2003): Theoretical evaluation of hydrogen storage capacity in pure carbon nanostructures. *J. Chem. Phys.*, vol. 119, pp. 2376–2385.

Liu, C.; Fan, Y. Y.; Liu, M.; Cong, T. H.; Cheng, H. M.; Dresselhaus, M. S. (1999): Hydrogen storage in single-walled carbon nanotubes at room temperature. *Science*, vol. 286, pp. 1127–1129.

Miura, Y.; Kasai, H.; Diño, W. A.; Nakanishi, H.; Sugimoto, T. (2003): First principles studies on the interaction of a hydrogen atom with a single-walled carbon nanotube. *Jpn. J. Appl. Phys.*, vol. 42, pp. 4626–4629.

Nakano, H.; Ohta, H.; Yokoe, A.; Doi, K.; Tachibana, A. (2006): First-principle molecular-dynamics study of hydrogen adsorption on an aluminum-doped carbon nanotube. *J. Power Sources*, vol. 163, pp. 125–134.

Nishimiya, N.; Ishigaki, K.; Takikawa, H.; Ikeda, M.; Hibi, Y.; Sakakibara, T.; Matsumoto, A.; Tsutsumi, K. (2002): Hydrogen sorption by single-walled carbon nanotubes prepared by a torch arc method. *J. Alloys Compd.*, vol. 339, pp. 275–282.

Okamoto, Y.; Miyamoto, Y. (2001): *Ab initio* investigation of physisorption of molecular hydrogen on planar and curved graphenes. *J. Phys. Chem. B*, vol. 105, pp. 3470–3474.

Patchkovskii, S.; Tse, J. S.; Yurchenko, S. N.; Zhechkov, L.; Heine, T.; Seifert, G. (2005): Graphene nanostructures as tunable storage media for molecular hydrogen. *Proc. Nat. Acad. Sci. U.S.A.*, vol. 102, pp. 10439–10444.

Rappé, A. K.; Casewit, C. J.; Colwell, K. S.; Goddard III, W. A.; Skiff, W. M. (1992): UFF, a full periodic table force field for molecular mechanics and molecular dynamics simulations. *J. Am. Chem. Soc.*, vol. 114, pp. 10024–10035.

Riedl, C.; Coletti, C.; Iwasaki, T.; Zakharov, A. A.; Starke, U. (2009): Quasi-free-standing epitaxial graphene on SiC obtained by hydrogen intercalation. *Phys. Rev. Lett.*, vol. 103, pp. 246804–1–246804–4.

Riedl, C.; Coletti, C.; Starke, U. (2010): Structural and electronic properties of epitaxial graphene on SiC(0001): a review of growth, characterization, transfer doping and hydrogen intercalation. *J. Phys. D: Appl. Phys.*, vol. 43, pp. 374009–1–374009–15.

Schmitt, U. W.; Voth, G. A. (1998): Multistate empirical valence bond model for proton transport in water. *J. Phys. Chem. B*, vol. 102, pp. 5547–5551.

Sha, X.; Jackson, B. (2001): First-principles study of the structural and energetic properties of H atoms on a graphite (0001) surface. *Surf. Sci.*, vol. 496, pp. 318–330.

Ströbel, R.; Jörissen, L.; Schliermann, T.; Trapp, V.; Schütz, W.; Bohmhammel, K.; Wolf, G.; Garche, J. (1999): Hydrogen adsorption on carbon materials. *J. Power Sources*, vol. 84, pp. 221–224.

Szabo, A.; Ostlund, N. S. (1982): *Modern Quantum Chemistry*. Macmillan Publishing, New York.

Tada, K.; Furuya, S.; Watanabe, K. (2001): *Ab initio* study of hydrogen adsorption to single-walled carbon nanotubes. *Phys. Rev. B*, vol. 63, pp. 155405–1–155405–4.

Virojanadara, C.; Yakimova, R.; Zakharov, A. A.; Johansson, L. I. (2010): Large homogeneous mono-/bi-layer graphene on 6H-SiC(0001) and buffer layer elimination. *J. Phys. D: Appl. Phys.*, vol. 43, pp. 374010–1–374010–13.

Virojanadara, C.; Zakharov, A. A.; Yakimova, R.; Johansson, L. I. (2010): Buffer layer free large area bi-layer graphene on SiC(0001). *Surf. Sci. Lett.*, vol. 604, pp. L4–L7.

Warshel, A.; Weiss, R. M. (1980): An empirical valence bond approach for comparing reactions in solutions and in enzymes. *J. Am. Chem. Soc.*, vol. 102, pp. 6218–6226.

Witmer, E. E. (1926): Critical potentials and the heat of dissociation of hydrogen as determined from its ultra-violet band spectrum. *Proc. Nat. Acad. Sci. U.S.A.*, vol. 12, pp. 238–244.

Xu, W.-C.; Takahashi, K.; Matsuo, Y.; Hattori, Y.; Kumagai, M.; Ishiyama, S.; Kaneko, K.; Iijima, S. (2007): Investigation of hydrogen storage capacity of various carbon materials. *Int. J. Hydrogen Energy*, vol. 32, pp. 2504–2512.

Yang, R. T. (2000): Hydrogen storage by alkali-doped carbon nanotubes-revisited. *Carbon*, vol. 38, pp. 623–641.

PHYSICAL REVIEW E **84**, 011805 (2011)

Characterization of polymer structures based on Burnside's lemma

Kentaro Doi, Keigo Kato, and Satoyuki Kawano*
Department of Mechanical Science and Bioengineering, Graduate School of Engineering Science, Osaka University, Osaka 560-8531, Japan
(Received 23 August 2010; published 19 July 2011)

Polymer structure modeling is a trend of recent material sciences. Developments of computational science and nanotechnology make it possible to predict properties of complicated molecular structures. Many theoretical and computational methods have succeeded in elucidating the nature of polymer structures. It is not always best to model whole complicated structures depending on computer capabilities. Significant properties of materials may be manifested in simple structural aspects. In the present study, characteristics of a polymer structure are investigated by applying Burnside's lemma to the modeling procedure. This method is expected to be available to model polymers or molecular crystals in which functional groups play an important role in expressing their functions. Every structure under the symmetry and periodicity is counted completely and the energy distribution caused by the conformations of functional groups can be clarified. The detailed procedure is introduced and the present method is applied to a problem for investigating molecular structures of sulfonated poly(ether ether ketone) (SPEEK). SPEEK is focused on a candidate for proton exchange membranes in polymer electrolyte fuel cells. Sulfonic groups have a significant role in proton exchange membranes to make proton conduction channels. From our analysis, it is found that sulfonic groups tend to be dispersed in SPEEK membranes at their stable conditions. These are unfavorable characteristics for proton exchange membranes due to their difficulty to form desirable water channels inevitable for the high proton conductivity. This is one reason why SPEEK membranes are inferior to Nafion® membranes that express the highest performance as proton exchange membranes. Using the present method, experimental and theoretical results previously reported are confirmed and detailed characteristics are discussed in terms of structural simplicities.

DOI: 10.1103/PhysRevE.84.011805 PACS number(s): 82.35.−x, 82.45.Wx, 81.07.−b, 82.47.Gh

I. INTRODUCTION

Recently, electron-conducting polymers and ion-conducting polymers have been attracting much attention [1–10]. They express various functions due to their specific structures or orientations of functional groups. In the case of electron-conducting polymers, overlaps of π orbitals above aromatic molecular surfaces enhance electronic conduction. Conformations of aromatic molecules strongly influence electronic conductivities. It is very important to control the molecular orientations in the fabrication processes. In ion-conducting polymers, carrier ions pass through water channels aggregated around functional groups. Especially in the case of proton conduction, protons appear to conduct through the water channels, changing the role of charge carrier with other H atoms of H_2O such as $H_3O^+ + H_2O \rightarrow H_2O + H_3O^+$. This mechanism is well known as the Grotthuss mechanism [11–18]. In this process, distributions of water molecules that concentrate around functional groups in polymers affect the proton conduction properties. Therefore, conformations of functional groups cause the formation of water channels that enhance high proton conduction. It is clear that molecular conformations significantly contribute to carrier conductivities in electron-conducting or ion-conducting polymers. However, there is a difficulty to modeling these polymers due to their complicated structures. In addition, it may be difficult to understand the origin of functions expressed by polymers even if their structures are modeled precisely.

On the other hand, some characteristics of polymers can be understood by simplified models. It is important to construct effective models from various perspectives to elucidate the mechanism. For instance, in the hopping conduction mechanism, it is suggested that electric carriers conduct through electronically or ionically polarized spaces. Therefore, it is meaningful to focus on an essence of carrier hopping process in polymer structures. Several methods to model polymer structures have been developed focusing on the behavior of functional groups [19–21]. Klein *et al.* [22–24] successfully counted and investigated molecular structures of alkane polymers. In their methods, Pólya's counting procedures were applied to investigate the polymer structures. In the present study, an original method is developed to model polymer structures focusing on functional groups that critically contribute to proton conduction. Our method assumes symmetries and periodicity to the polymer structures, although direct modeling of complicated molecular structures is a usual method. Using an imaginary polymer model, fundamental characteristics expressed by functional groups are discussed. In a closed symmetric system, all structures can be counted and the qualitative characteristics are elucidated from the energy distribution. This problem is treated as the similar way of color paintings on tiles.

In such procedures, energetically equivalent structures can be eliminated from all permutations based on the group theory. As a result, the computational efficiency is drastically improved compared with sequential counting of all possible permutations. The present method is applied to sulfonated poly(ether ether ketone) (SPEEK). In SPEEK membranes, sulfonic groups have a significant role in making proton

*kawano@me.es.osaka-u.ac.jp; http://bnf.me.es.osaka-u.ac.jp

conduction channels [25–34]. Water molecules aggregate around sulfonic groups that are hydrophilic and enhance proton conduction. However, further proton conductivity and mechanical strength are required for the proton exchange membranes to endure the hard use under extraordinary conditions, such as fuel cells in electric vehicles. It is important to clarify the possibility of the materials. In the present model, one- and two-dimensional symmetric geometries in polymer bundles are treated. Energy distributions about molecular conformations are computed and the relationship between the structural stability and functional group conformations are clarified. In particular, it is found that sulfonic groups in SPEEK tend to be dispersed at their stable conditions and that concentrations of sulfonic groups that contribute to make water channels cannot be expected. On the other hand, bundles of the polymer chains tend to be energetically stable. The results derived from our mathematical approach reasonably agree with other computational results [35–38].

II. THEORETICAL DEVELOPMENT AND COMPUTATIONAL METHOD

In symmetric closed systems, structure modeling can be replaced by a tile painting problem. For example, Fig. 1 shows colored tiles that are sequentially aligned on a periodic band. These tiles are painted by four colors, such as red (R), green (G), blue (B), and yellow (Y). Considering the periodicity, symmetry equivalent colorings should be eliminated to count the number of nonequivalent colorings exactly. In order to treat this problem, there is an effective calculus based on the group theory and Burnside's lemma [39–43]. As shown in Fig. 1, the characteristics of a band are conserved under the symmetric operations, such as rotation, reflection, inversion, and their coupled operations, although color patterns seem to be changed by the operations. When each tile is painted by one of four colors, the number of nonequivalent patterns will be much less than that of all the combinations in which any symmetries and any boundary conditions are not considered. According to Burnside's lemma, the number of nonequivalent colorings under any symmetry can be counted mechanically.

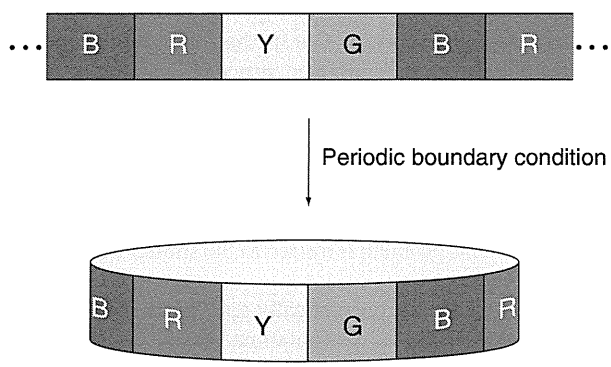

FIG. 1. (Color online) Illustration of color paintings by four colors, red (R), green (G), blue (B), and yellow (Y), on a one-dimensional segment, which is transformed to a band manifesting the periodicity.

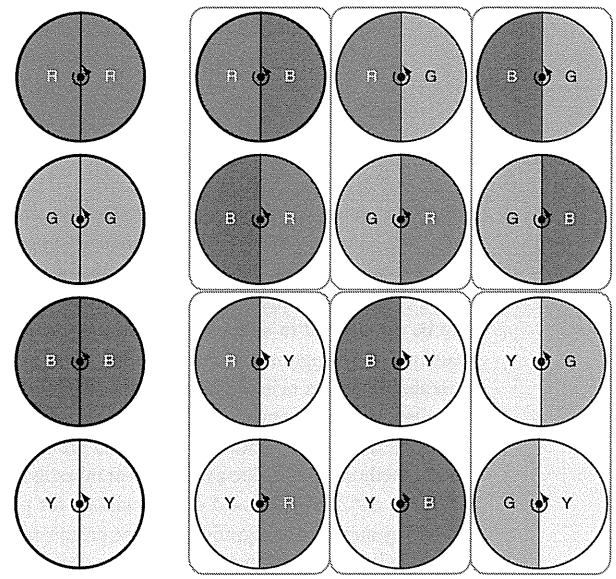

FIG. 2. (Color online) Painting on C_2 symmetric structure by (a) plain color and (b) two colors.

Burnside's lemma proves that the number of nonequivalent colorings N in a set C equals the average of the number of colorings fixed by the permutations in a group G [42]:

$$N(G) = \frac{1}{|G|}\sum_{f\in G}|C(f)|, \tag{1}$$

where C is a set of colorings such that $f * \mathbf{c} \in C$ for all symmetric operations $f \in G$ and all $\mathbf{c} \in C$. For example, characteristics are invariant under rotations in the cyclic group C_n when there are n tiles. In a C_2 symmetric structure as shown in Fig. 2, the principal rotational axis is perpendicular to the surface. There are 10 nonequivalent colorings to paint two parts of the surface due to four patterns by four plain colors and due to six patterns by two colors calculated from the combination of ${}_4C_2$. On the other hand, in accordance with Burnside's lemma, the number is counted simply as follows:

$$\begin{aligned} N(C_2) &= \frac{1}{\text{the number of symmetric operations}} \\ &\quad \times [(\text{colorings conserved by identical operation } E) \\ &\quad + (\text{colorings conserved by } C_2 \text{ rotation})] \\ &= \frac{1}{2}(4^2+4) = 10. \end{aligned} \tag{2}$$

That is, equivalent colorings which have six overlaps in this case are systematically eliminated from all the permutation: $4^2 = 16$. Furthermore, in a C_6 symmetric structure, nonequivalent colorings by four colors can be counted exactly:

$$\begin{aligned} N(C_6) &= \tfrac{1}{6}\left[C(E) + C(C_6) + C\left(C_6^2\right)\right. \\ &\quad \left. + C\left(C_6^3\right) + C\left(C_6^4\right) + C\left(C_6^5\right)\right] \\ &= \tfrac{1}{6}(4^6 + 4 + 4^2 + 4^3 + 4^2 + 4) = 700. \end{aligned} \tag{3}$$

TABLE I. Counts of four color paintings on a symmetric band: all permutation of 4^n, nonequivalent N colorings according to C_n symmetry based on Burnside's lemma, and their ratio. (n: number of tiles; N: number of colorings.)

	n					
	2	4	6	8	10	12
4^n	16	256	4960	65 536	1 048 596	16 777 216
$N(C_n)$	10	70	700	8230	104 968	1 398 500
$N(C_n)/4^n$	0.63	0.27	0.14	0.13	0.10	0.08

This number of nonequivalent colorings is much less than that of all the permutations 4^6 (= 4960) such that their ratio is 0.14 ($\simeq$ 700/4960). Table I shows some comparisons between the nonequivalent colorings and all permutations for C_n symmetry. It is found that the ratio of nonequivalent colorings to all permutations is drastically reduced, e.g., the reduction ratio $N(C_n)/4^n \simeq 0.1$ for $n > 10$. This result indicates that the elimination of equivalent permutations is very effective in reducing the computational labor.

In this study, one- and two-dimensional molecular sequences are featured. Figure 3 shows monomer structures which are elements of SPEEK. It is assumed that the monomer structure is planar and that there are four conformations of sulfonic groups in the polymer chain. In other words, a sulfonic group is placed in one of four parts of the unit cell. The problem of counting the monomer sequences can be replaced by a four color painting problem. In order to simplify the complicated polymer structures, symmetries and periodicities are adjusted, focusing on the relative location of sulfonic groups. A monomer is packed in a unit cell; the cell parameters are set to $a_1 = 8.682$ Å, $a_2 = 5.643$ Å, and $a_3 = 17.040$ Å along the x, y, and z axis, respectively. These parameters are determined to eliminate the intermolecular repulsions and to minimize the total energy. The polymer structure is constructed from combinations of these conformations. The present system has D_{nh} symmetry, which shows n-fold rotations about the principal axis, twofold rotations about the perpendicular axes, reflections in planes containing the principal axis, the reflection in the plane normal to the principal axis represented by the subscript h, and the inversion. In this case, the counting process seems to be complicated due to an increase in the number of symmetry operations, but the basic procedure is the same as that mentioned above based on Burnside's lemma, e.g., Eqs. (1)–(3). In the next section, results from counting up every nonequivalent n-mer chain are presented. Two-dimensional matrices in SPEEK bundles are discussed focusing on the relationship between conformations of sulfonic groups and their energy stabilities. The total energy of a system is evaluated using potential energy functions as follows [44–50]:

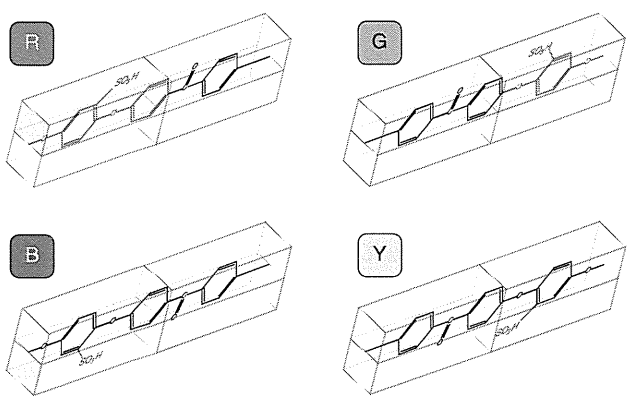

FIG. 3. (Color online) Illustrations of four conformations of the sulfonic group in SPEEK; the monomer is assumed to be a planar molecule on the xz plane and the main chain is along the z axis.

$$U_{\text{total}} = U_{\text{intra}} + U_{\text{inter}}, \tag{4}$$

$$U_{\text{intra}} = \sum^{N_r} K_r(r - r_{\text{eq}})^2 + \sum^{N_\theta} K_\theta(\theta - \theta_{\text{eq}})^2 + \sum^{N_d} \frac{V_n}{2}[1 + \cos(n\phi - \gamma)], \tag{5}$$

$$U_{\text{inter}} = \sum_{i<j}^{N_a} \left(\frac{A_{ij}}{R_{ij}^{12}} - \frac{B_{ij}}{R_{ij}^{6}} \right) + \sum_{i<j}^{N_a} \frac{q_i q_j}{4\pi\varepsilon_0 R_{ij}}, \tag{6}$$

where U_{intra} and U_{inter} denote intramolecular and intermolecular interactions, respectively. In the U_{intra}, bond energies are calculated for N_r bonds in which K_r is the force constant and $r - r_{\text{eq}}$ is the difference from the equivalent bond length; energies depending on bond angles are calculated for N_θ angles in which K_θ is the force constant and $\theta - \theta_{\text{eq}}$ is the difference from the equivalent angle; energies depending on dihedral angles are evaluated for N_d dihedral angles in which V_n is a force constant and $n\phi - \gamma$ is the difference from the equivalent angle. In the U_{inter}, the first and second terms respectively denote van der Waals (VDW) interactions and Coulomb interactions for N_a atoms, where R_{ij} is the distance between nuclei, A_{ij} and B_{ij} the constants depending on ion pairs, q_i the valence charge, and ε_0 the vacuum permittivity. A monomer structure of sulfonated ether ether ketone is optimized by summing the potential functions of Eqs. (5) and (6). In particular, intermolecular interactions between the polymer chains are evaluated by VDW and Coulomb interactions according to Eq. (6) and their computations are carried out for a minimal size of the supercell. As a schematic of the supercell is shown in Fig. 4(a), conformations of sulfonated ether ether ketone in the supercell are represented. The convergence of the intermolecular interactions is evaluated by

$$\delta_n = \frac{E_{\text{inter}}(n+1) - E_{\text{inter}}(n)}{E_{\text{inter}}(n) - E_{\text{inter}}(n-1)} - 1, \tag{7}$$

where $E_{\text{inter}}(n)$ denotes the energy of a system that consists of n unit cells. The energy convergence is determined by $|\delta_n| < \epsilon$ for integer m such that $n > m$. The energy evaluation is performed for finite systems without considering periodicities to directly estimate the effective range of intermolecular interactions. These evaluations are summarized in Table II. In this study, the small value ϵ is set to 0.05 and then the supercell is determined as the integral multiple of the unit cells: $(n_x, n_y, n_z) = (3,3,1)$ as shown in Fig. 4. Intermolecular interactions along the polymer main chain (z axis) are so weak that conformations of sulfonic groups are not effective for intermolecular interactions along the z axis. Therefore,

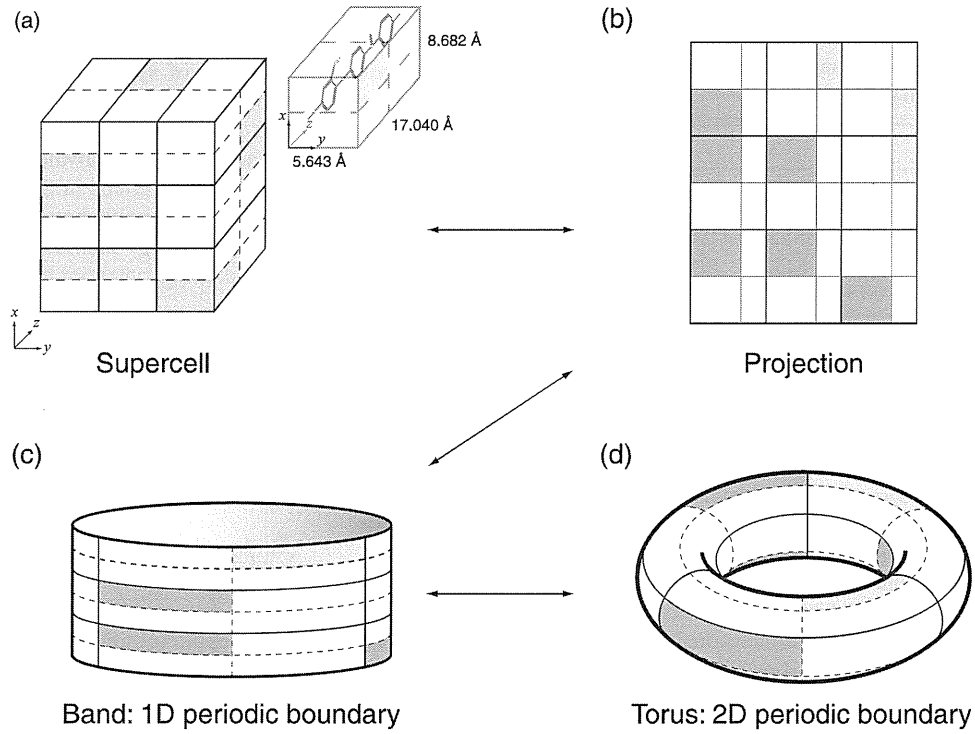

FIG. 4. Schematic illustrations of continuous transformations between (a) supercell, (b) projection on a plane, (c) band, and (d) torus.

conformations of the sulfonic groups in the vertical plane (xy plane) dominate energy stabilities. The intermolecular energy evaluations are performed with a three-dimensional periodic boundary condition. Figure 4 shows a concept of topological transformation of the supercell. Figure 4(b) is a projection of the supercell [Fig. 4(a)] onto the xy plane. Here, structural characteristics are attributed to the sulfonic group conformations in a two-dimensional plane, such as a cross section of the polymer chain bundle. Focusing on four conformations of a sulfonic group, $D_{3h} \times D_{3h}$ symmetry is applied to count up all the nonequivalent structures. As shown in Figs. 4(b)–4(d), the two-dimensional periodic structure is represented by the torus symmetry that is continuously transformed from the two-dimensional plane.

TABLE II. Intermolecular interaction energy, the difference, and convergence.

	$E_{\text{inter}}(n)$ (kJ/mol)	$E_{\text{inter}}(n) - E_{\text{inter}}(n-1)$ (kJ/mol)	δ_n
n_x			
2	−387	−387	0.118
3	−820	−433	0.002
4	−1254	−433	
n_y			
2	−387	−387	0.152
3	−833	−446	0.015
4	−1285	−452	
n_z			
2	−387	−387	0.005
3	−774	−389	

III. RESULTS AND DISCUSSION

Table III shows the number of nonequivalent four-color paintings counted according to D_{nh} symmetry. First, calculations for one-dimensional periodic sequences shown in Fig. 1 were carried out. For comparison, the ratio of $N(D_{nh})/4^n$ is also presented in Table III. It is found that the number of nonequivalent sequences increases exponentially and the increase is approximately presented as a function of n: $2^{1.7n-2.3}$. This counting method based on Burnside's lemma is more efficient than counting all the permutations. The ratio becomes the order of 10^{-2} for $n > 3$. Computational labor can be drastically reduced using the effective counting procedure in the symmetric structures.

Next, conformations of functional groups in two-dimensional matrices are investigated. Sulfonic groups in the supercell composed of $3 \times 3 \times 1$ unit cells are treated and their distributions are counted completely according to D_{3h} symmetry. As mentioned above, this thing can be replaced by a problem to count the number of ways of tile colorings on the 3×3 periodic matrix. This two-dimensional periodic matrix of $D_{3h} \times D_{3h}$ symmetry is topologically transformed to a torus symmetry as shown in Fig. 4. Figure 5 shows the principal axes of $C1$ and $C2$ in the torus symmetry. Rotations along $C1$ and $C2$ correspond to periodic translations along the y and x axis of the supercell, respectively. The group order is provided by tensor products of each vector space. In the same way as the one-dimensional case, nonequivalent structures can be counted completely. The number of nonequivalent structures is concluded to be 7296, which is much less than 4^9 (= 262 144). Intermolecular energy computations for the nonequivalent structures were performed. Figure 6

TABLE III. Nonequivalent counts according to D_{3h} symmetry and proportion to permutation of 4^n.

	n														
	1	2	3	4	5	6	7	8	9	10	11	12	13	14	15
$N(D_{nh})$	1	4	6	23	52	194	586	2131	7285	26 524	95 326	350 738	1 290 556	4 798 174	17 895 703
$N(D_{nh})/4^n$	0.25	0.25	0.09	0.09	0.05	0.05	0.04	0.03	0.03	0.03	0.02	0.02	0.02	0.02	0.02

shows the relationship between the polymer structures and the intermolecular energies. For comparison, the total energies of the nonequivalent molecular structures were computed using molecular mechanics (MM) method [48]. The abscissa shows the sequential number that is sorted by the energies resulting from MM computations. The results from the present computations are corrected by the energy shift. The computational accuracy of MM methods is higher than that of the present method, although more computational time is consumed, because all intermolecular and intramolecular interactions are counted and the long-range intermolecular interactions are considered up to the cutoff distances: 10 Å for VDW interactions and 30 Å for Coulomb interactions [44–50]. Therefore, the difference between the MM and our results was corrected by the energy shift. The mean energies were estimated from each energy distribution, such as $\overline{E}$ resulting from the present study and $\overline{E}_{\mathrm{MM}}$ from MM computations. The difference between the two was calculated as

$$\overline{E} - \overline{E}_{\mathrm{MM}} = \frac{1}{N}\sum_{i=1}^{N} E_i - \frac{1}{N}\sum_{i=1}^{N} E_{\mathrm{MM},i} = \frac{1}{N}\sum_{i=1}^{N}(E_i - E_{\mathrm{MM},i}) \equiv \overline{\Delta E}, \tag{8}$$

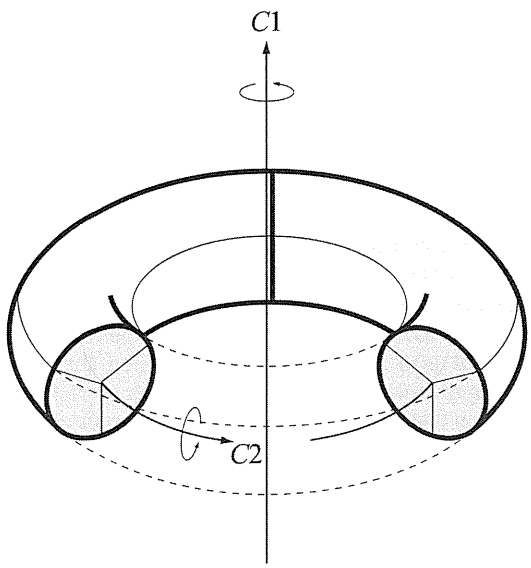

FIG. 5. Torus of two-dimensional D_{3h} symmetry, which represents the 3×3 matrix; $C1$ and $C2$ are principal axes of each vector space.

where $N = 7296$ and $\overline{\Delta E}$ was estimated as 1268 kJ/mol. As a result of the parallel shift, the present result was in good agreement with the result of MM computations. The distribution is clearly represented by our simple procedure. The difference between the two is caused by the long-range intermolecular interactions ignored out of the nearest neighbors in the present method. However, this ignorance is not so serious to maintain the qualitative characteristics. The present computations, which include intermolecular interactions only between the nearest neighbors, can represent the characteristics resulting from more laborious methods.

Figure 7 shows the energy distributions depending on sulfonic group conformations. For comparison, results from MM computations are presented in the same figure. The difference between each distribution was corrected by the procedure mentioned above. Shapes of these energy distributions showing peaks between −9000 and −6000 kJ/mol agreed with each other. It is clear that nonequivalent stable or unstable structures are relatively fewer than energetically intermediate structures. The whole picture of structural stability can be clarified using the present method. Structural characteristics are statistically elucidated, although discussions are constrained by the symmetry. Figure 8 shows schematic illustrations of sulfonic group conformations. As shown in Fig. 8(a), each block indicates positions of sulfonic groups along the z axis: front upper, front lower, rear upper, and rear lower sides. A part including a sulfonic group is painted in a gray color. As shown in Fig. 8(b), polymer structures become unstable as their conformations are highly oriented. This tendency is

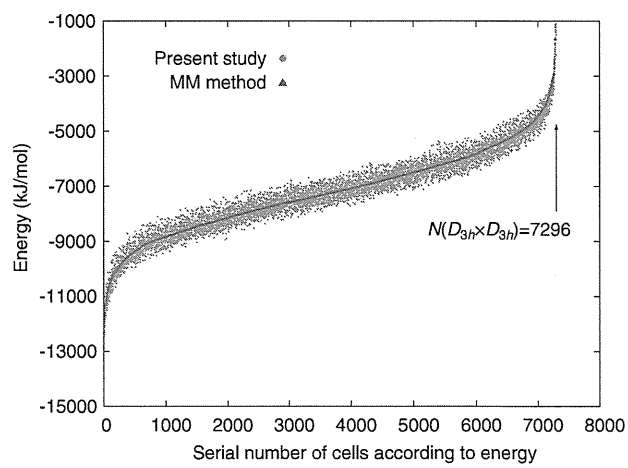

FIG. 6. (Color online) Comparison of energies between the present method (closed purple circle) and MM method (closed blue triangle); plots of the present result are shifted by 1268 kJ/mol each.

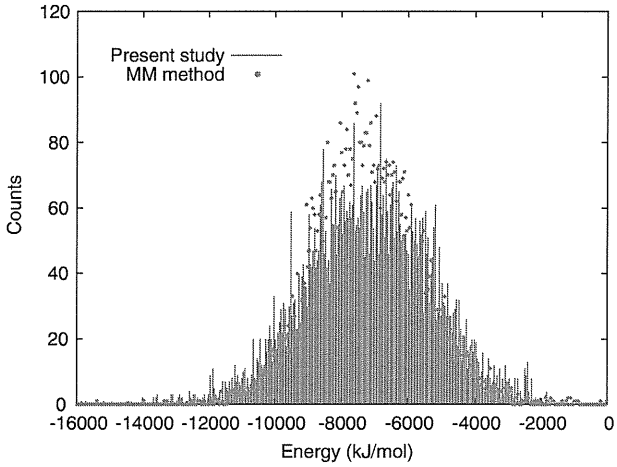

FIG. 7. (Color online) Energy distribution of $3 \times 3 \times 1$ nonequivalent periodic structures of the SPEEK model; the present results are shifted by 1268 kJ/mol each.

remarkable at the highest 10% of the energy distribution. However, the polymer chains tend to be attractive by their intermolecular interactions. Therefore, SPEEK is stable with forming the polymer chain bundles. At intermediate energy regions as shown in Figs. 8(c) and 8(d), partial concentrations or sparse regions of sulfonic groups are observed in various polymorphisms. This variety contributes to the high population in the distribution and they are nonequivalent to each other. On the other hand, as shown in Figs. 8(e) and 8(f), in the lowest 10% of the energy distribution, sulfonic groups are stabilized in polymer bundle structures and, in this case, they tend to be located to avoid concentrations. It is clarified that, in the case of SPEEK, sulfonic groups usually avoid their concentrations, although bundles of the polymer chains make their structures energetically stable.

Figure 9 shows the radial distribution functions of sulfonic groups in SPEEK. The function is evaluated by

$$g(r) = \frac{\overline{N(r)}}{4\pi r^2 \rho \Delta r}, \tag{9}$$

where $\overline{N(r)}$ is the number of sulfonic groups in a spherical shell between r and $r + \Delta r$, which is averaged over each energy region; ρ is the density of sulfonic groups in SPEEK. Distances between sulfur atoms in sulfonic groups were measured. The thickness of the spherical shell Δr was set to 0.85 Å. The value of ρ was set to 8.47×10^{-2} g/cm^3, as determined from the optimized unit cell. As shown in Fig. 9, the radial distribution functions were calculated for several regions in the energy distribution. The low-, high-, and intermediate-energy regions correspond to those shown in Fig. 7. In the high-energy structures, sulfonic groups concentrate at a distance of 5.5 Å. In addition, the second and third nearest peaks are at 7.2 and 8.9 Å, respectively. Amounts of the second and third nearest-neighbor sulfonic groups are fewer than those of the nearest one. However, peaks at a long distance seem to be affected by the periodicity. In particular, peaks out to $r = 8.46$ Å may contain the effect of the periodicity due to the half-length of the shortest side 16.92 Å along the y axis on the

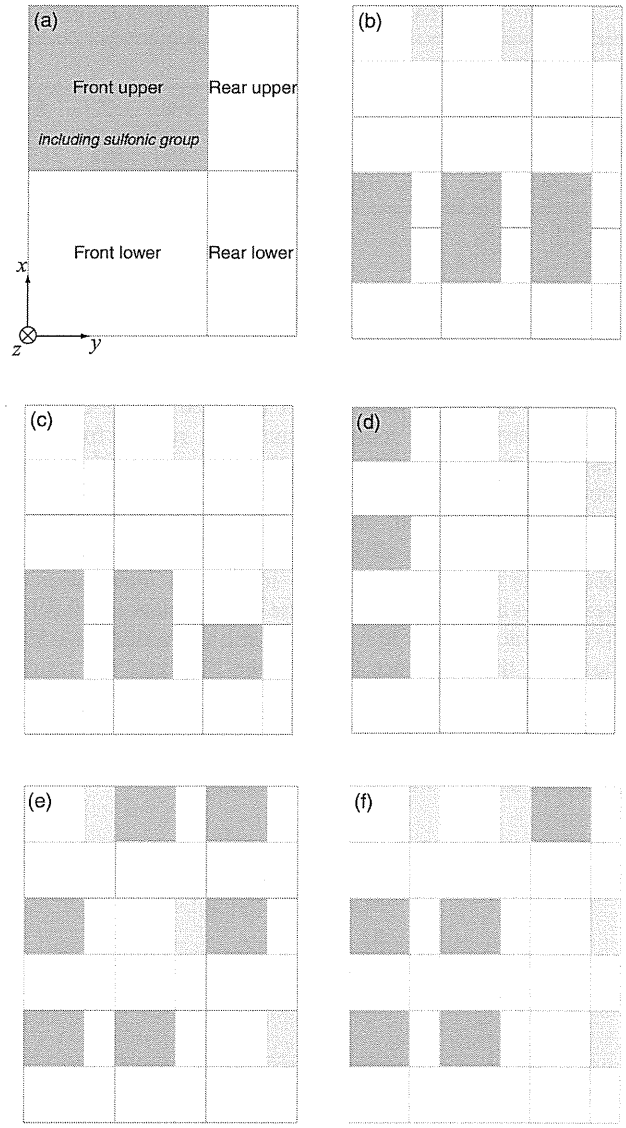

FIG. 8. (a) Schematic of sulfonic group conformation in SPEEK, (b) the high-energy placements, (c), (d) energetically intermediate conformations, and (e), (f) the low-energy conformations.

supercell. Therefore, discussions are especially focused on the first and second peaks of $g(r)$. The radial distribution of the low-energy structures shows that the first and second nearest peaks are observed at 5.5 and 7.2 Å, respectively. These points are the same as those of high-energy structures. However, quantities of $g(r)$ are different depending on the structural stability. In the low-energy structures, a peak of 15.9 at 5.5 Å is lower than that of 22.9 in the high-energy structures. On the other hand, the second peak of 13.8 at 7.2 Å is higher than that of 11.6 in the high-energy structures. The distribution of the intermediate-energy region, which is focused on 10% around the peak of distribution, is similar to that of the low-energy region, although the values at the first and second peaks are a little larger than those in the case of low-energy structures. From Fig. 9, the relationship between the energy stabilities and the distributions of sulfonic groups is elucidated. These results

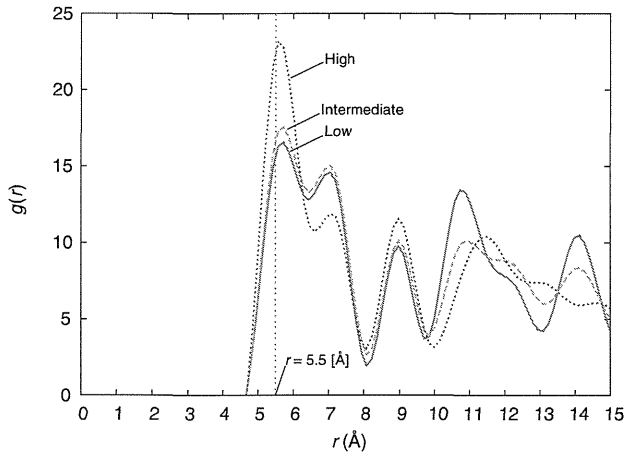

FIG. 9. (Color online) Radial distribution functions of sulfonic groups in $3 \times 3 \times 1$ periodic structures of SPEEK: analyses for 10% of the lowest (solid red line), intermediate (dashed green line), and highest energy structures (dotted blue line). These plots are interpolated by cubic spline. The peak point at $r = 5.5$ Å reasonably agrees with other results in Refs. [35] and [37].

indicate that the systems become stable as sulfonic groups are located sparsely. In addition, highly oriented placements and high concentrations of sulfonic groups in SPEEK make the polymer structures relatively unstable. These distribution characteristics of sulfonic groups correspond to the schematic visualizations in Fig. 8. Furthermore, the radial distribution functions are in agreement with results from other researchers using the coarse-grained [35] and atomistic [37] molecular dynamics methods. In the real polymer structures, it is implied that main chains are concentrated locally with cross-linking and that sulfonic groups are distributed stably in these domains. In addition, in other computational methods depending on a concept of structural optimization, the relatively unstable orientations resulting from our method cannot be obtained.

In this study, a counting method of molecular structures is featured and effects of temperature and pressure on the polymer structures have not been considered. However, the present method is effectively applied to predict molecular structures in molecular dynamics simulations or Monte Carlo methods, in which free energies depending on temperature and pressure are computed.

SPEEK is expected to be a preferable candidate for a proton exchange membrane due to mechanical strength and thermal stability [25,26,30,32]. However, the proton conductivity is known to be inferior to a major proton exchange membrane Nafion®. In Nafion® membranes, sulfonic groups that contribute to form water channels can flexibly move for their reorientations when water molecules are injected. Water channels are inevitable to enhance the proton conduction. On the other hand, sulfonic groups in SPEEK are directly bonded to main chains and there are no side chains that effectively contribute to the reorientations. In this study, the present method is applied to investigate the possibility of SPEEK forming a preferable structure to make water channels. Consequently, our results indicate that sulfonic groups tend to be distributed homogeneously in SPEEK and that concentrated water channels cannot be expected. Therefore, sufficient humidification is required to form water channels in SPEEK. This suggestion qualitatively confirms the experimental and computational results from SPEEK membranes [27–29,33,34,36,38].

IV. CONCLUDING REMARKS

In the present study, a theoretical procedure to model polymer structures was developed under the assumptions of the symmetry and the periodicity. Based on Burnside's lemma, the number of nonequivalent structures in a symmetric system was counted efficiently, eliminating energetically equivalent structures. A tile painting problem was applied to calculate nonequivalent polymer structures. Computations were performed for one- and two-dimensional alignments and the computational efficiency was improved.

This method was applied to investigate a role of functional groups in polymers. Significant characteristics could be obtained focusing on the distribution of functional groups, although the complexity of the polymer structures was ignored.

Distributions of sulfonic groups in SPEEK were counted completely on the assumption of D_{3h} symmetry. Consequently, it was found that sulfonic groups tend to be dispersed in the polymer structures and that highly oriented structures become unstable relatively. Sulfonic group concentrations that induce water channels to promote proton conduction are predicted to be unfavorable in SPEEK. These results conclude that enough humidification is required to obtain high proton conductivity using SPEEK membranes. On the other hand, the energy stability of the polymer chain bundles indicates the mechanical stability of SPEEK.

[1] F. J. M. Hoeben, P. Jonkheijm, E. W. Meijer, and A. P. H. J. Schenning, Chem. Rev. **105**, 1491 (2005).
[2] K. Doi, K. Yoshida, H. Nakano, A. Tachibana, T. Tanabe, Y. Kojima, and K. Okazaki, J. Appl. Phys. **98**, 113709 (2005).
[3] H. B. Akkerman, P. W. M. Blom, D. M. de Leeuw, and B. de Boer, Nature (London) **441**, 69 (2006).
[4] M. Taniguchi and T. Kawai, Physica E **33**, 1 (2006).
[5] M. Armand and J. M. Tarascon, Nature (London) **451**, 652 (2008).
[6] S. Lu, J. Pan, A. Huang, L. Zhuang, and J. Lu, Proc. Natl. Acad. Sci. USA **105**, 20611 (2008).
[7] K. Doi, K. Kato, and S. Kawano, in *Proceedings of the International Conference on Computational & Experimental Engineering and Sciences, Las Vegas, 2010*, edited by D. W. Pepper and S. N. Atluri (Tech Science Press, Las Vegas, 2010), pp. 330–335.
[8] K. Doi, T. Yonebayashi, and S. Kawano, J. Mol. Struct., Theochem. **939**, 97 (2010).
[9] J. E. Yoo, K. S. Lee, A. Garcia, J. Tarver, E. D. Gomez, K. Baldwin, Y. Sun, H. Meng, T. Q. Nguyen, and Y. L. Loo, Proc. Natl. Acad. Sci. USA **107**, 5712 (2010).

[10] K. Tybrandt, K. C. Larsson, A. Richter-Dahlfors, and M. Berggren, Proc. Natl. Acad. Sci. USA **107**, 9929 (2010).
[11] N. Agmon, Chem. Phys. Lett. **244**, 456 (1995).
[12] D. Marx, M. E. Tuckerman, J. Hutter, and M. Parrinello, Nature (London) **397**, 601 (1999).
[13] U. W. Schmitt and G. A. Voth, J. Chem. Phys. **111**, 9361 (1999).
[14] N. Agmon, Chem. Phys. Lett. **319**, 247 (2000).
[15] M. E. Tuckerman, D. Marx, and M. Parrinello, Nature (London) **417**, 925 (2002).
[16] H. Lapid, N. Agmon, M. K. Petersen, and G. A. Voth, J. Chem. Phys. **122**, 014506 (2005).
[17] J. Han, X. Zhou, and H. Liu, J. Power Sources **161**, 1420 (2006).
[18] J. A. Elliott and S. J. Paddison, Phys. Chem. Chem. Phys. **9**, 2602 (2007).
[19] S. S. Jang, V. Molinero, T. Çağin, and A. G. William III, J. Phys. Chem. B **108**, 3149 (2004).
[20] D. Brandell, J. Karo, A. Liivat, and J. O. Thomas, J. Mol. Model. **13**, 1039 (2007).
[21] K. Malek, M. Eikerling, Q. Wang, Z. Liu, S. Othuka, K. Akizuki, and M. Abe, J. Chem. Phys. **129**, 204702 (2008).
[22] L. Bytautas and D. J. Klein, J. Chem. Inf. Model. **38**, 1063 (1998).
[23] L. Bytautas and D. J. Klein, J. Chem. Inf. Model. **39**, 803 (1999).
[24] A. Misra and D. J. Klein, J. Chem. Inf. Model. **42**, 1171 (2002).
[25] T. Kobayashi, M. Rikukawa, K. Sanui, and N. Ogata, Solid State Ion. **106**, 219 (1998).
[26] S. M. J. Zaidi, S. D. Mikhailenko, G. P. Robertson, M. D. Guiver, and S. Kaliaguine, J. Membr. Sci. **173**, 17 (2000).
[27] K. D. Kreuer, J. Membr. Sci. **185**, 29 (2001).
[28] S. D. Mikhailenko, K. Wang, S. Kaliaguine, P. Xing, G. P. Robertson, and M. D. Guiver, J. Membr. Sci. **233**, 93 (2004).
[29] B. Yang and A. Manthiram, J. Power Sources **153**, 29 (2006).
[30] J. Chen, M. Asano, Y. Maekawa, and M. Yoshida, J. Membr. Sci. **319**, 1 (2008).
[31] J. K. Lee, W. Li, and A. Manthiram, J. Power Sources **180**, 56 (2008).
[32] G. Zhang, T. Fu, K. Shao, X. Li, C. Zhao, H. Na, and H. Zhang, J. Power Sources **189**, 875 (2009).
[33] J. C. Tsai, H. P. Cheng, J. F. Kuo, Y.-H. Huang, and C.-Y. Chen, J. Power Sources **189**, 958 (2009).
[34] S. D. Mikhailenko, F. Celso, and S. Kaliaguine, J. Membr. Sci. **345**, 315 (2009).
[35] E. Spohr, J. Mol. Liq. **136**, 288 (2007).
[36] P. Y. Chen, C. P. Chiu, and C. Hong, J. Power Sources **194**, 746 (2009).
[37] C. V. Mahajan and V. Ganesan, J. Phys. Chem. B **114**, 8357 (2010).
[38] C. V. Mahajan and V. Ganesan, J. Phys. Chem. B **114**, 8367 (2010).
[39] N. G. Bruijn, J. Comb. Theory **2**, 418 (1967).
[40] E. M. Wright, J. Combin. Theory Ser. B **30**, 89 (1981).
[41] K. P. Bogart, Am. Math. Mon. **98**, 927 (1991).
[42] R. A. Brualdi, *Introductory Combinatorics*, 5th ed. (Pearson Prentice Hall, Upper Saddle River, NJ, 2010), pp. 552–558.
[43] Burnside's lemma is also known as the Cauchy-Frobenius theorem. Details about the origin, the historical transition, and its applications to chemical compounds are mentioned in several books: G. Pólya and R. C. Read, *Combinatorial Enumeration of Groups, Graphs, and Chemical Compounds* (Springer-Verlag, New York, 1987), pp. 96–135; A. Kerber, *Applied Finite Group Actions*, 2nd ed. (Springer-Verlag, Berlin Heidelberg, 1999), pp. 53–73.
[44] S. Kawano, Phys. Rev. E **58**, 4468 (1998).
[45] S. Nagahiro, S. Kawano, and H. Kotera, Phys. Rev. E **75**, 011902 (2007).
[46] I. Hanasaki, T. Haga, and S. Kawano, J. Phys. Condens. Matter **20**, 255238 (2008).
[47] I. Hanasaki, H. Takahashi, G. Sazaki, K. Nakajima, and S. Kawano, J. Phys. D: Appl. Phys. **41**, 095301 (2008).
[48] D. A. Case *et al.*, computer code AMBER 10, University of California, San Francisco, 2008.
[49] I. Hanasaki, H. Shintaku, S. Matsunami, and S. Kawano, Comput. Model. Eng. Sci. **46**, 191 (2009).
[50] K. Doi, T. Haga, and S. Kawano, Phil. Trans. R. Soc. A **368**, 2615 (2010).

Hearing Research 283 (2012) 117–125

Contents lists available at SciVerse ScienceDirect

Hearing Research

journal homepage: www.elsevier.com/locate/heares

Research paper

Effects of a perilymphatic fistula on the passive vibration response of the basilar membrane

Takuji Koike [a,*], Chiaki Sakamoto [a], Tasuku Sakashita [a], Ken Hayashi [b], Sho Kanzaki [c], Kaoru Ogawa [c]

[a] Department of Mechanical Engineering and Intelligent Systems, Graduate School of Informatics and Engineering, The University of Electro-Communications, 1-5-1 Chofugaoka, Chofu, Tokyo 182-8585, Japan
[b] Department of Otolaryngology, Shinkawa Clinic, Kanagawa, Japan
[c] Department of Otolaryngology, School of Medicine, Keio University, Tokyo, Japan

ARTICLE INFO

Article history:
Received 13 July 2010
Received in revised form
8 October 2011
Accepted 22 October 2011
Available online 15 November 2011

ABSTRACT

In this study, a three-dimensional finite-element model of the passive human cochlea was created. Dynamic behavior of the basilar membrane caused by the vibration of the stapes footplate was analyzed considering a fluid–structure interaction with the cochlear fluid. Next, the effects of a perilymphatic fistula (PLF) on the vibration of the cochlea were examined by making a small hole on the wall of the cochlea model. Even if a PLF existed in the scala vestibuli, a traveling wave was generated on the basilar membrane. When a PLF existed at the basal end of the cochlea, the shape of the traveling wave envelope showed no remarkable change, but the maximum amplitude became smaller at the entire frequency range from 0.5 to 5 kHz and decreased with decreasing frequency. In contrast, when a PLF existed at the second turn of the cochlea, the traveling wave envelope showed a notch at the position of the PLF and the maximum amplitude also became smaller. This model assists in elucidating the mechanisms of hearing loss due to a PLF from the view of dynamics.

1. Introduction

The mammalian cochlea consists of a fluid-filled duct that is coiled like a snail shell. The cochlea is divided into three compartments, i.e., the scala vestibuli, the scala media, and the scala tympani, by two longitudinal membranes, i.e., Reissner's membrane and the basilar membrane (BM). The vibration of the tympanic membrane (TM), which is induced by sound, is transmitted to the cochlear fluid through the ossicular chain. The vibration of the cochlear fluid generates a traveling wave on the BM. Auditory sensory cells, which are lined up on the BM, also vibrate in response to the vibration of the BM. The sensory cells transform the vibration of the BM into action potentials in auditory nerve fibers. Therefore, the vibration of the BM is closely related to auditory activity. Ren (2002) achieved vibration measurement of the BM under normal physiological conditions. However, observation of the entire vibration of the BM under physiological conditions is difficult because the bony wall of the cochlea surrounds the BM. To estimate the vibration of the BM under physiological conditions in detail, some theoretical studies have investigated the vibration of the BM using the Wentzel–Kramers–Brillouin (WKB) method (Steele and Taber, 1979; Lim and Steele, 2002; Yoon et al., 2007) or the finite-element method (Böhnke and Arnold, 1999; Manoussaki and Chadwick, 2000; Parthasarathi et al., 2000; Andoh et al., 2005; Skrodzka, 2005; Ramamoorthy et al., 2007; Meaud and Grosh, 2010; Fleischer et al., 2010).

A perilymphatic fistula (PLF) entails pathological connections between the perilymphatic space of the labyrinth and the middle ear (outer fistula) or the cerebrospinal fluid (inner fistula). These abnormal connections clinically have been considered to lead to hearing loss. Indeed, the round window (RW) and oval window (OW) fistula are frequently observed diseases resulting in hearing loss (Goto et al., 2001). However, Weisskopf et al. (1978) noted that hearing loss experimentally was not caused by the leakage of perilymphatic fluid alone. Therefore, the potential causes of this hearing loss associated with PLF have been postulated to include: a double-membrane break (Simmons, 1979), a floating labyrinth (Nomura and Hara, 1986; Nomura et al., 1992), a perilymphatic hemorrhage (Merchant et al., 2005), a pneumolabyrinth (Nishioka and Yanagihara, 1986; Foster and Luebke, 2002), a bony third window (Merchant and Rosowski, 2008) as well as from other

Abbreviations: BM, basilar membrane; CF, characteristic frequency; FE, finite element; IHC, inner hair cells; OHC, outer hair cells; OW, oval window; PLF, perilymphatic fistula; RW, round window; ST, scala tympani; SV, scala vestibuli; TM, tympanic membrane.

* Corresponding author. Tel./fax: +81 42 443 5818.
E-mail address: koike@mce.uec.ac.jp (T. Koike).

0378-5955/$ – see front matter © 2011 Elsevier B.V. All rights reserved.
doi:10.1016/j.heares.2011.10.006

causes. However, the mechanisms that lead to hearing loss in these matters are unclear.

In this study, the dynamic behavior of the BM and the cochlear fluid caused by the vibration of the stapes were analyzed using a three-dimensional finite-element model of the human cochlea, and the effects of a fistula on the vibration of the BM were analyzed.

2. Model

2.1. Geometry

Fig. 1 shows a Finite-Element (FE) model of the human cochlea. Although the cochlear takes a spiral form, the shape of the FE model was straightened out. As a preliminary investigation, a spiral-shaped model was made, and the results were compared to those obtained from the straight model. The points of maximum amplitude on the BM in the spiral-shaped model were shifted to the basal region by 6% (at high frequencies) to 10% (at low frequencies) compared with those in the straight model. The peak amplitude in the spiral-shaped model was reduced by up to 6% at low frequencies. Although slight changes were observed, the difference in the vibration behavior of the BM between the two models was not in general remarkable. Therefore, to avoid complications of the analysis, the straight model is used in this paper.

The straight model consists of structural parts and liquid parts. The structural parts are the stapes, the stapedial annular ligament, the OW membrane, the RW membrane, the BM, and the osseous spiral lamina. The liquid parts are the vestibule, the scala vestibuli, the scala tympani, and the cochlear aqueduct, which are all filled with lymphatic fluid. To avoid complication of the analysis, the structures in the cochlea were simplified as follows. Although the inner hair cells (IHC), the outer hair cells (OHC), and supporting cells exist on the BM, these cells were ignored, and the BM was assumed to be a thin flat membrane. Accordingly, the active cochlear mechanism of amplification related to the electromotility of the OHCs was not included. Reissner's membrane was also ignored in this model, and the lymphatic fluid area was divided into two compartments by the BM and the osseous spiral lamina. These two liquid compartments, i.e., the scala vestibuli and the scala tympani, were connected at the helicotrema. The scala vestibuli and the scala tympani were considered as rectangular ducts, and the outer shape of the cochlea was assumed to change linearly from base to apex.

The volume of the lymphatic fluid, the width and thickness of the BM, the area and thickness of the RW membrane were determined based on data previously reported (Ulehlova et al., 1987; Igarashi et al., 1986; Becvarovski, 2004; Wever, 1949; Koike et al., 2002). Specifically, regarding the shape of the BM, its width was assumed to be 100 μm at the basal part and 500 μm at the apex, and to change linearly from base to apex. In the same way, its thickness was assumed to be 30 μm at the basal part and 10 μm at the apex. The dimensions of the cochlear model are summarized in Fig. 2 and Table 1.

2.2. Mechanical properties and boundary conditions

The mechanical properties of each part of the model were determined based on previous reports (Andoh and Wada, 2004; Koike et al., 2002; Lim et al., 2005). The reported value of the Young's modulus of the BM was slightly modified so that our numerical results correspond with the measurements results. Young's modulus for the RW membrane was assumed to be the same as that of the TM (Koike et al., 2002). In the previous study (Koike et al., 2002), a simple stapes model consisting of only the stapes, stapedial annular ligament, and loading of the cochlea damping was established, and Young's modulus for the stapedial annular ligament was determined so that the impedance of the stapes corresponds with the measurement result of the stapes impedance (Merchant et al., 1996). In this study, the OW membrane was newly considered, and the values of the unknown mechanical properties of the OW membrane were determined to optimize the impedance of the stapes. However, the contribution of the stiffness of the OW membrane is much smaller than that of the annular ligament because the OW membrane is thinner than the annular ligament. In addition, because the thickness of the OW membrane is unclear, the mechanical properties of the OW membrane may have margins of error.

Rayleigh damping parameters affect the shape of the traveling wave. The parameters were determined so that the envelope of the traveling wave was similar to the measurement results (Ren, 2002). The BM consists of collagen fibers embedded in a ground substance and appears to be an anisotropic material (Iurato, 1962; Cabezudo, 1978; Schweitzer et al., 1996; Dreiling et al., 2002). Fleischer et al. (2010) reported that spatial variation in the compliance of the BM in both the longitudinal and radial directions is partially caused by the anisotropy. However, the BM is considered to be an isotropic material in this model. The mechanical properties used for the model are summarized in Table 2.

The extremities of the BM, the RW membrane, and the stapedial annular ligament were rigidly fixed. Because the real cochlea is embedded in the temporal bone, the walls of the vestibule, the scala vestibuli and the scala tympani were assumed to be rigid walls. At the end of the cochlear aqueduct on the subarachnoid space side, the pressure fluctuation caused by the stapes vibration was assumed to be negligible, and the boundary condition for the

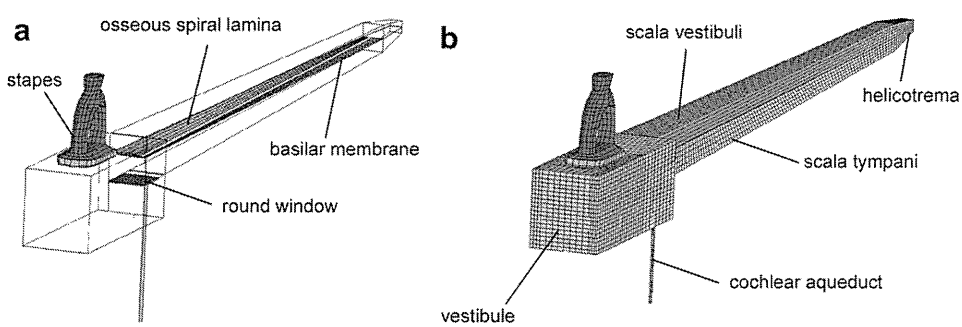

Fig. 1. Finite-element model of the human cochlea. (a) Structural parts. (b) Liquid parts. The OW membrane covers the OW and sticks to the flat surface of the stapes footplate. The OW membrane, the RW membrane, and the BM were meshed by four-noded shell elements. Other parts were meshed by eight-noded hexahedral elements. The total numbers of the nodes and elements were 41,912 and 28,393, respectively.